

Metals and Molecules in the Distant Universe: Magellan MIKE Observations of Gas-rich Galaxies at $2 < z < 3$

Suraj Poudel,¹[★] Varsha P. Kulkarni,¹ Debopam Som,² Céline Péroux^{3,4}

¹*University of South Carolina, Dept. of Physics and Astronomy, 712 Main Street, Columbia, SC 29208, USA*

²*Space Telescope Science Institute, 3700 San Martin Drive, Baltimore, MD 21218, USA*

³*European Southern Observatory, Karl-Schwarzschild-Strasse 2, 85748 Garching bei Munchen, Germany*

⁴*Laboratoire d'Astrophysique de Marseille, UMR 7326, F-13388, Marseille, France*

Accepted XXX. Received YYY; in original form ZZZ

ABSTRACT

We present abundance measurements of the elements Zn, S, O, C, Si and Fe for four sub-DLAs at redshifts ranging from $z=2.173$ to $z=2.635$ using observations from the MIKE spectrograph on the Magellan telescope in order to constrain the chemical enrichment and star formation of gas-rich galaxies. Using weakly depleted elements such as O, S, and or Zn, we find the metallicities after the photoionization corrections to be $[S/H]=-0.50\pm0.11$, $[O/H]=-0.70\pm0.17$, $[O/H]=-1.27\pm0.12$, and $[Zn/H]=+0.40\pm0.12$ for the absorbers at $z=2.173$, 2.236, 2.539, and 2.635, respectively. Moreover, we are able to put constraints on the electron densities using the fine structure lines of C II[★] and Si II[★] for two of the sub-DLAs. We find that these values are much higher than the median values found in DLAs in the literature. Furthermore, we estimate the cooling rate $l_c=1.20\times10^{-26}$ erg s⁻¹ per H atom for an absorber at $z=2.173$, suggesting higher star formation rate density in this sub-DLA than the typical star formation rate density for DLAs at similar redshifts. We also study the metallicity versus velocity dispersion relation for our absorbers and compare the values with those from the literature. Most of the absorbers follow the trend one can expect from the mass versus metallicity relation for sub-DLAs. Finally, we are able to put limits on the molecular column density from the non detections of various strong lines of CO molecules. We estimate 3σ upper limits of $\log N_{COJ0}<13.68$ and $\log N_{COJ0}<14.05$, respectively, from the non-detections of COJ0 $\lambda 1477.6$ and COJ0 $\lambda 1544.4$ lines.

Key words: ISM: abundances – galaxies: high-redshift – quasars: absorption lines

1 INTRODUCTION

Since molecular clouds, formed out of the cold neutral clouds are the birthplaces of stars, neutral gas is key to the formation of stars and galaxies. Absorption lines in quasar spectra offer a promising tool to measure the chemical properties of neutral gas in distant galaxies. DLAs (Damped Lyman-alpha Absorbers) and sub-DLAs (sub-Damped Lyman-alpha Absorbers) in background quasar spectra, which have high neutral hydrogen column densities ($\log N_{HI} \geq 20.3$ and $19.0 \leq \log N_{HI} < 20.3$, respectively), together dominate the neutral gas mass density of the universe at high redshift (e.g. Péroux et al. 2003b; Wolfe et al. 2005; Zafar et al. 2013; Berg et al. 2019) and provide the neutral gas reservoirs for star formation (e.g. Nagamine et al. 2004a,b; Wolfe & Chen. 2006). Moreover,

this absorption-line technique samples galaxies independent of their brightness, and is not limited to only the bright or actively star forming galaxies (SFGs). In fact, DLAs/sub-DLAs are less affected by photoionization compared to the Lyman Limit Systems (LLSs) and are thus better suited for estimating the metallicity in order to study the interplay between neutral gas and the newly formed stars in the interstellar medium in the high-redshift Universe.

While extensive studies of sub-DLA/DLA metallicity evolution have been carried out in the past (e.g. Kulkarni & Fall 2002; Prochaska et al. 2003a; Kulkarni et al. 2005, 2007; Rafelski et al. 2012; Jorgenson et al. 2013; Som et al. 2013, 2015; Quiret et al. 2016; Poudel et al. 2018, 2019), a great deal remains unknown about the role they play in star formation and galaxy formation. The metallicities, relative abundances, and gas kinematics of DLAs/sub-DLAs provide important clues

[★] E-mail: spoudel@email.sc.edu

about the star formation history. Moreover, the snapshots of galaxy features provided by DLAs/sub-DLAs are crucial for constraining the comoving densities of gas and metals and their evolution (e.g. Kulkarni et al. 2007). In fact, many sub-DLAs are known to be more metal rich than typical DLAs, and may originate from galaxies of different masses (e.g. Khare et al. 2007; Kulkarni et al. 2010). Therefore, DLAs and sub-DLAs may have different nucleosynthetic histories, and possibly exhibit different star formation rates. The higher average metallicity of sub-DLAs also suggests that they may have higher dust content and thus provide better conditions for the formation of molecules than DLAs.

Wolfe et al. (2004) suggested that DLAs are heated by radiation fields generated by a limited range of star formation rates per unit area, between 10^{-3} to 10^{-2} M_{\odot} yr^{-1} kpc^{-2} . These values were estimated from C II \star column densities in a sample of 45 DLAs in the redshift interval 1.6 to 4.5. However, these values for sub-DLAs remain largely unexplored. Samples of thousands of DLAs are available (e.g. Noterdaeme et al. 2012), however, sub-DLAs remain little studied. In fact, high spectral resolution and high signal-to-noise ratio (SNR) data are needed to derive the element abundances in sub-DLAs owing to their smaller H I column densities compared to DLAs. High spectral resolution is also needed to resolve the C II \star λ 1336 line without blending with the nearby C II λ 1334 line, which is usually strongly saturated. Moreover, study of the closely spaced molecular lines associated with the vibrational and rotational bands of H₂ and CO require high spectral resolution. The Magellan Inamori Kyocera Echelle (MIKE) spectrograph on the Magellan (Clay) telescope provides high enough resolution ($R \sim 22,000$ – $28,000$) to resolve the C II \star λ 1336 as well as the molecular lines of CO.

Here, we present a study of the metallicities, electron densities and star formation rates for a sample of 4 sub-DLAs observed at high resolution with the MIKE spectrograph on the Magellan (Clay) telescope. Moreover, we search for the molecular lines and put limits in the column densities of CO. This paper is organized as follows: section 2 presents our observations and details of data reduction. Section 3 describes our techniques for measurements of the column densities and determination of the element abundances. Section 4 describes the results for the individual absorbers. Section 5 presents a discussion of our results. Finally, section 6 summarizes our conclusions.

2 OBSERVATIONS AND DATA REDUCTION

Our sample consists of four absorbers with neutral hydrogen column densities ranging from $\log N_{\text{HI}} = 19.00$ to 20.05, at redshifts 2.173 to 2.635 along the sight lines to three quasars. These quasars were observed with the MIKE spectrograph on the Magellan Clay telescope at Las Campanas observatory in Chile as a part of NOAO program 2010A-0499 (PI Kulkarni). Observations were carried out with the 1×5 arcsec² slit which resulted in a spectral resolution of $\sim 22,000$ with the red arm and $\sim 28,000$ with the blue arm. While the blue arm has a wavelength coverage of 3400 to 4900 Å, the red arm has a wavelength coverage

of 4900 to 9400 Å. The sightlines were observed in multiple exposures, to facilitate the rejection of cosmic rays. The details of the observations are summarized in Table 1.

The data reduction was performed using the MIKE pipeline reduction code written in IDL and developed by S. Burles, J. X. Prochaska and R. Bernstein. The reduction package makes use of the overscan region to perform bias subtraction and then flat fields the data. The pipeline then performs sky-subtraction and extracts the spectral orders using the traces from flat-field images. The code then performs the wavelength calibration using the Th-Ar comparison lamp exposures, taken before and after each science exposure. It also corrects for heliocentric velocities and converts the wavelengths to vacuum. After extracting each individual echelle order, we used IRAF to combine corresponding orders from multiple exposures using rejection parameters to reduce the effects of cosmic rays. Finally the spectra were normalized using spline or Legendre polynomials, typically with order of 4 or 5 to fit the quasar continuum.

3 VOIGT PROFILE FITTING AND ABUNDANCE MEASUREMENTS

The Voigt profile fitting program VPFIT¹ v. 10.0 was used for the determination of column densities of all detected atoms and ions. The program minimizes the χ^2 residual between the data and theoretical Voigt profiles convolved with the instrumental line spread profile using multiple iterations. The Doppler b parameters and redshifts of the corresponding components were tied together to perform simultaneous multi-component Voigt profile fitting of multiple lines of multiple ions.

All of our spectra have high enough resolution (10 to 14 km s⁻¹) to resolve the blending of metal lines. In most of the cases, we were able to use multiple lines to minimize the possible error caused by saturation (e.g. Penprase et al. 2010). One of the problems even with these intermediate-redshift systems is the possible blending of metal lines with hydrogen lines in the Lyman- α forest. However, our column density values are robust as most of the lines used for the column density determinations are outside the Lyman- α forest. Further details are provided in the description of the results for individual absorbers in Section 4.

In all cases, the H I column densities were estimated by fitting Voigt profiles to the Lyman- α lines adopting the absorber redshifts as determined from the profile fits to the metal-lines. The other Lyman-series lines beyond Lyman- α could not be measured, mostly because the spectra do not cover these lines, and partly because of blending with the Lyman- α forest features. The uncertainties in the H I column densities were estimated by comparing different fitted profiles with the observed data so that the differences are within the 2σ noise level.

¹ <https://www.ast.cam.ac.uk/rfc/vpfit.html>

To estimate the abundance of each element X, we used the relation, $[X/H] = \log(N_X/N_{\text{HI}}) - \log(X/H)_\odot$, where N_X is the column density of element X, N_{HI} is the neutral hydrogen column density and $\log(X/H)_\odot$ is the solar abundance of the element X. Solar photospheric values were adopted from [Asplund et al. \(2009\)](#). Finally, the rest-frame wavelengths and oscillator strengths were adopted from [Morton \(2004\)](#) and [Cashman et al. \(2017\)](#).

4 RESULTS FOR INDIVIDUAL ABSORBERS

In this section, we report the results for individual absorbers derived from Voigt profile fitting. We report the column densities of all detected atoms and ions, inferred absolute and relative abundances, and the gas kinematics determined from velocity dispersion measurements. For each system, the H I Lyman- α lines are shown in Fig. 1.

4.1 Absorber at $z = 2.173$ along the sight line to J1106-1731

The sight line to J1106-1731 probes a sub-DLA at a redshift of $z=2.173$. For this system, we determine the H I column density to be $\log N_{\text{HI}} = 20.05 \pm 0.10$. We analyzed the metal lines in this system by performing Voigt profile fitting for S II $\lambda 1260$, Si II $\lambda 1808$, Si II $\lambda 1304$, Fe II $\lambda 2250$, and Fe II $\lambda 2261$. While the O I $\lambda 1302$ and C II $\lambda 1334$ lines were heavily saturated, we were able to estimate lower limits on O I and C II column densities. The C II* $\lambda 1336$ line was also detected which together with the lower limit on C II column density, allowed us to estimate the cooling rate as well as a limit on the electron density. Fig. 2 shows the Voigt profile fits for the metal lines and the results from the fits are shown in Table 2. This system is a metal-rich sub-DLA with $[S/H] = -0.50 \pm 0.11$.

4.2 Absorber at $z = 2.539$ along the sight line to J1106-1731

The sight line to J1106-1731 probes a second sub-DLA at a redshift of $z=2.539$. For this absorber, we determine the H I column density to be $\log N_{\text{HI}} = 19.00 \pm 0.12$. We analyzed this system by performing Voigt profile fitting for O I $\lambda 1302$, Si II $\lambda 1304$, Si II $\lambda 1808$, Fe II $\lambda 1608$, Fe II $\lambda 2250$, Al II $\lambda 1671$, Al III $\lambda 1855$, Al III $\lambda 1863$, and Si IV $\lambda 1394$. Fig. 3 and Fig. 4 show the Voigt profile fits for the lower and higher ions respectively. The results from the fits are shown in Table 3 and Table 4 respectively. This system has an ionization-corrected metallicity of $[O/H] = -1.27 \pm 0.12$ (See section 5.1 below for details about ionization corrections).

4.3 Absorber at $z = 2.635$ along the sight line to J1244+1129

The sight line to J1244+1129 probes a sub-DLA at a redshift of $z=2.635$. For this absorber, we determine the H I column density to be $\log N_{\text{HI}} = 19.50 \pm 0.12$. We performed Voigt profile fitting for O I $\lambda 1302$, Si II $\lambda 1527$, Fe II $\lambda 1608$, Fe II $\lambda 2374$, Al II $\lambda 1671$, S II $\lambda 1260$, Zn II

$\lambda 2026.1$, Zn II $\lambda 2062.7$, Al III $\lambda 1855$, Al III $\lambda 1863$, and Si IV $\lambda 1394$. Fig. 5 and Fig. 6 show the Voigt profile fits for the detected atoms and ions. The results from the fits are shown in Table 5 and Table 6. We note that Zn II $\lambda 2026.1$ and Zn II $\lambda 2062.7$ absorptions are very weak. However, the ionization-corrected value of $[Zn/H] = 0.40 \pm 0.12$ is consistent with those of $[O/H]$, $[Si/H]$, and $[Al/H]$ (see Table 10).

4.4 Absorber at $z = 2.236$ along the sight line to J1614+1448

The sight line to J1614+1448 probes a sub-DLA at a redshift of $z=2.236$. For this absorber, we determine the H I column density to be $\log N_{\text{HI}} = 19.75 \pm 0.10$. We performed Voigt profile fitting for O I $\lambda 1302$, Si II $\lambda 1304$, Si II $\lambda 1808$, Fe II $\lambda 1608$, Fe II $\lambda 1145$, Fe II $\lambda 1143$, Al II $\lambda 1671$, Al III $\lambda 1855$, and Al III $\lambda 1863$. The Si II* $\lambda 1264$, Si II* $\lambda 1265$, and Si II* $\lambda 1533$ lines were also detected which together with the Si II column density, allowed us to put constraints on the electron densities. Fig. 7, Fig. 8, and Fig. 9 show the Voigt profile fits for the detected atoms and ions. The results from the fits are listed in Table 7 and in Table 8. This system is a fairly metal-rich sub-DLA with ionization-corrected metallicity of $[O/H] = -0.70 \pm 0.17$.

5 DISCUSSION

We now discuss the implications of our results for various aspects of chemical enrichment processes. We compare our results with those from the literature and discuss the trends in metallicity evolution, dust, relative abundances, and constraints on electron densities. Moreover, we discuss the photoionization, star formation rate density, and search for molecules in sub-DLAs.

5.1 Photoionization

For systems consisting of both H I and H II regions, the ionized gas needs to be taken into account while determining element abundances. The gas in the high H I column density absorbers is usually expected to be largely neutral due to the self-shielding of photons. Therefore, these ionization corrections are usually ignored for DLAs. However, ionization corrections may not always be small for sub-DLAs, given their somewhat lower H I column densities. Past studies suggest that corrections to element abundances due to ionization are generally $\lesssim 0.2$ dex for sub-DLAs (e.g. [Dessauges-Zavadsky et al. 2003](#); [Meiring et al. 2009](#); [Cooke et al. 2011](#); [Som et al. 2015](#)). We have performed ionization corrections for three sub-DLAs in our sample using the plasma simulation code Cloudy v. 13.03 (e.g. [Ferland et al. 2013](#)). For the sub-DLA at $z=2.173$ that has relatively high H I column density ($\log N_{\text{HI}} = 20.05 \pm 0.10$), we have not performed any photoionization corrections as lines of higher ions are not available to place constraints on the ionization parameter.

In each case, the absorbing gas was assumed to be a

Table 1. Summary of targets and observations

Quasar Name	z_{em}	z_{abs}	$\log N_{\text{HI}}$ (cm^{-2})	Exposure Time (s)	Wavelength Coverage(\AA)	Spectral Resolution (R)
J1106-1731	2.572	2.173 2.539	20.05 \pm 0.10 19.00 \pm 0.12	7200	3,500-9,400	Red: 22,000 Blue: 28,000
J1244+1129	3.153	2.635	19.50 \pm 0.12	5400	3500-9,400	Red: 22,000 Blue: 28,000
J1614+1448	2.548	2.236	19.75 \pm 0.10	5400	3500-9,400	Red: 22,000 Blue: 28,000

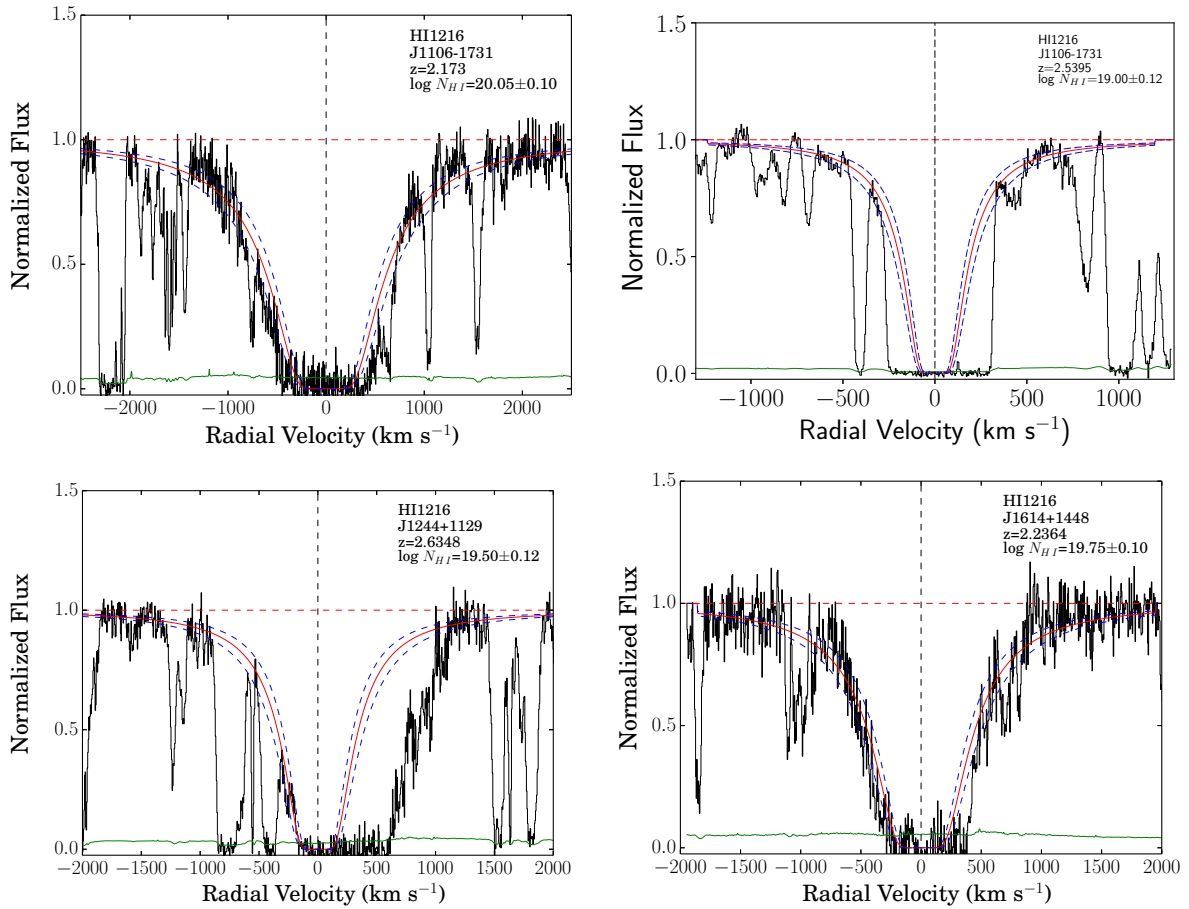


Figure 1. Voigt profile fitting for hydrogen Lyman- α for all the absorbers. In each case, the observed quasar continuum-normalized flux is shown in black and the best fitted profile is shown in red. The blue dashed curves above and below the fitted profile represent the uncertainty in the column density determination. The 1σ error in the normalized flux is shown in green at the bottom of each panel. The centre of the profile is shown as a black dashed line. The placement of continuum is shown by the horizontal dashed red line. The names of the quasars, redshifts, and $\log N_{\text{HI}}$ values are listed in the top right corner of each panel.

slab of constant density, illuminated by a radiation field consisting of a mixture of an extragalactic background and the cosmic microwave background at the redshift of the absorber. The extragalactic background was adopted from Khaire & Srianand (2019) which emphasizes the extreme ultraviolet (UV) background that is responsible for the observed ionization and thermal state of the intergalactic medium across cosmic time. Moreover, these models use updated values of the star formation rate density and

dust attenuation in galaxies, QSO emissivity, and the distribution of H I gas in the intergalactic medium. In addition, the cosmic ray background was also included in our simulation. While the observed $\frac{\text{AlIII}}{\text{AlII}}$ ratio was used to constrain the ionization parameter $U = \frac{n_{\gamma}}{n_{\text{H}}}$ (the ratio of the number density of ionizing photons to that of neutral hydrogen) for all the systems. In addition, for two cases, we also used the observed $\frac{\text{SiIV}}{\text{SiII}}$ ratio.

Table 2. Results of Voigt profile fitting for different elements in the $z_{\text{abs}} = 2.173$ absorber along the sight line to J1106-1731.

z	b_{eff} (km s $^{-1}$)	$\log N_{\text{OI}}$	$\log N_{\text{SiII}}$	$\log N_{\text{FeII}}$	$\log N_{\text{SII}}$	$\log N_{\text{CII}}$	$\log N_{\text{CII}\star}$
2.172627	5.54 ± 1.14	...	13.98 ± 0.03	13.98 ± 0.17	13.6 ± 0.20		
2.172999	10.58 ± 2.09	...	14.72 ± 0.19	13.93 ± 0.21	13.7 ± 0.18		
2.173208	9.17 ± 1.09	...	13.84 ± 0.03				
2.173565	24.13 ± 1.63	...	14.98 ± 0.05	14.78 ± 0.04	14.58 ± 0.04		
2.173781	3.31 ± 0.63	...	14.23 ± 0.16				
2.174034	14.44 ± 2.65	...	13.86 ± 0.03				
2.174408	6.26 ± 2.14	...	13.85 ± 0.04		
Total log N	...	> 15.34	15.29 ± 0.06	14.89 ± 0.04	14.67 ± 0.04	> 15.11	13.67 ± 0.20
[O/H]	[Si/H]	[Fe/H]	[S/H]	[Si/S]	[C/H]		
> -1.40	-0.27 ± 0.12	-0.66 ± 0.11	-0.50 ± 0.11	0.23 ± 0.06	> -1.37		

Table 3. Results of Voigt profile fitting for different elements in the $z_{\text{abs}} = 2.539$ absorber along the sight line to J1106-1731.

z	b_{eff} (km s $^{-1}$)	$\log N_{\text{OI}}$	$\log N_{\text{SiII}}$	$\log N_{\text{FeII}}$	$\log N_{\text{AlII}}$
2.537499	20.06 ± 2.09	13.58 ± 0.08	13.16 ± 0.11		12.40 ± 0.07
2.538431	15.10 ± 2.14	13.18 ± 0.18	13.41 ± 0.06		12.41 ± 0.06
2.538660	2.27 ± 0.14	12.82 ± 0.30	13.48 ± 0.11		12.19 ± 0.27
2.539030	6.98 ± 2.14	13.50 ± 0.08	13.80 ± 0.03	13.24 ± 0.12	12.53 ± 0.08
2.539411	4.16 ± 1.14	13.27 ± 0.10	13.75 ± 0.05	13.05 ± 0.19	12.85 ± 0.19
2.539578	3.92 ± 1.14	13.87 ± 0.07	14.05 ± 0.08	13.08 ± 0.18	12.78 ± 0.21
2.539893	9.11 ± 1.63	13.72 ± 0.06	13.55 ± 0.04	13.09 ± 0.16	12.35 ± 0.07
2.540291	4.35 ± 1.14	13.04 ± 0.14	13.45 ± 0.06		12.06 ± 0.17
Total log N	...	14.39 ± 0.03	14.56 ± 0.03	13.72 ± 0.08	13.42 ± 0.07

Table 4. Results of Voigt profile fitting for different higher ions in the $z_{\text{abs}} = 2.539$ absorber along the sight line to J1106-1731.

z	b_{eff} (km s $^{-1}$)	$\log N_{\text{AlIII}}$	$\log N_{\text{SiIV}}$
2.53849	18.77 ± 1.14	12.46 ± 0.08	13.68 ± 0.11
2.53902	10.90 ± 2.09	12.48 ± 0.07	13.22 ± 0.16
2.53951	20.41 ± 1.63	12.90 ± 0.03	13.76 ± 0.12
2.54041	21.3 ± 2.14	12.33 ± 0.11	13.22 ± 0.12
Total log N	...	13.20 ± 0.03	14.14 ± 0.07

Table 5. Results of Voigt profile fitting for different elements in the $z_{\text{abs}} = 2.635$ absorber along the sight line to J1244+1129.

z	b_{eff} (km s $^{-1}$)	$\log N_{\text{SiII}}$	$\log N_{\text{AlII}}$	$\log N_{\text{FeII}}$	$\log N_{\text{ZnII}}$	$\log N_{\text{OI}}$	$\log N_{\text{SII}}$
2.633463	3.10	13.27 ± 0.09	12.43 ± 0.15				
2.633773	4.08	13.47 ± 0.07	12.41 ± 0.11				
2.634817	5.37	15.18 ± 0.11	14.15 ± 0.16	14.00 ± 0.06	11.91 ± 0.15	> 16.59	> 14.08
2.635429	6.71	12.95 ± 0.09	12.22 ± 0.07				
2.636147	8.36	13.42 ± 0.05	12.42 ± 0.06				
2.636751	29.3	13.95 ± 0.02	13.03 ± 0.02	13.62 ± 0.06	12.14 ± 0.14		
2.637263	3.66	13.10 ± 0.10	12.33 ± 0.13				
2.637958	12.25	13.38 ± 0.04	12.50 ± 0.04				
2.638413	3.83	13.29 ± 0.08	12.46 ± 0.11				
Total LogN		15.24 ± 0.10	14.23 ± 0.13	14.15 ± 0.05	12.34 ± 0.02	> 16.59	> 14.08
[O/H]	[Si/H]	[Fe/H]	[Al/H]	[Zn/H]			
> 0.40	0.23 ± 0.15	-0.85 ± 0.13	0.28 ± 0.18	0.28 ± 0.12			

Table 6. Results of Voigt profile fitting for different higher ions in the $z_{abs} = 2.635$ absorber along the sight line to J1244+1129.

z	b_{eff} (km s $^{-1}$)	$\log N_{\text{SiIV}}$	$\log N_{\text{AlIII}}$
2.633693	27.15 ± 1.14	12.96 ± 0.08	12.37 ± 0.06
2.636593	44.75 ± 1.63	13.19 ± 0.08	12.56 ± 0.07
2.637055	25.82 ± 2.14	13.02 ± 0.10	12.21 ± 0.12
2.637961	37.34 ± 2.09	13.21 ± 0.06	12.34 ± 0.08
Total log N	...	13.71 ± 0.04	12.99 ± 0.04

Table 7. Results of Voigt profile fitting for different elements in the $z_{abs} = 2.236$ absorber along the sight line to J1614+1448.

z	b_{eff} (km s $^{-1}$)	$\log N_{\text{AlII}}$	$\log N_{\text{OI}}$	$\log N_{\text{SiII}}$	$\log N_{\text{FeII}}$	$\log N_{\text{SiII}\star}$
2.235882 ± 0.00001	22.49 ± 2.09	12.56 ± 0.17	14.62 ± 0.06	13.92 ± 0.04	13.80 ± 0.08	12.06 ± 0.28
2.236239 ± 0.00012	11.49 ± 2.28					11.96 ± 0.34
2.236389 ± 0.00004	11.42 ± 1.14	13.29 ± 0.27	15.70 ± 0.15	14.69 ± 0.05	14.27 ± 0.06	12.33 ± 0.18
2.236824 ± 0.00007	11.49 ± 2.28					12.22 ± 0.22
2.237870 ± 0.00004	15.00 ± 1.63		13.75 ± 0.15	13.13 ± 0.17	13.92 ± 0.06	
2.238375 ± 0.00001	13.00 ± 2.14		14.06 ± 0.08	13.23 ± 0.13	13.12 ± 0.24	
Total log N	...	> 13.36	15.75 ± 0.13	14.78 ± 0.04	14.54 ± 0.04	12.77 ± 0.12
[O/H]	[Si/H]	[Fe/H]	[Si/O]			
-0.69 ± 0.17	-0.48 ± 0.11	-0.71 ± 0.11	0.21 ± 0.14			

Table 8. Results of Voigt profile fitting for higher ions in the $z_{abs} = 2.236$ absorber along the sight line to J1614+1448.

z	b_{eff} (km s $^{-1}$)	$\log N_{\text{AlIII}}$
2.236344	13.21 ± 1.1	12.70 ± 0.02

For the system at $z = 2.539$ with $\log N_{\text{HI}} = 19.00 \pm 0.12$, we used grids of models in the range $-1.0 > \log n_{\text{H}} > -3$, calculating the predicted column density ratio $\frac{\text{AlIII}}{\text{AlII}}$. Comparing this prediction to the observed Al III/Al II ratio gave $\log U = -2.49$ and $\log n_{\text{H}} = -2.4$ (see Fig. 10). The resultant ionization corrections to be applied ($\log \frac{N_{\text{Xtotal}}}{N_{\text{Htotal}}} - \log \frac{N_{\text{Xdominant}}}{N_{\text{Htotal}}}$, where, X is any element, $N_{\text{Htotal}} = N_{\text{HI}} + N_{\text{HII}} + N_{\text{HIII}} + \dots$) for various elements were then calculated. This implies ionization corrections of 0.03 dex for O, -0.87 dex for Si, -1.01 dex for Al, and -0.38 dex for Fe (see Table 9). The determination of the ionization correction for O was negligible (0.03 dex). This is expected, because the ionization potential of O I is very close to that of H I. We therefore regard the O abundance as the most reliable indicator of metallicity in this system. For the remaining elements, the ionization corrections seem quite high, which is not surprising as this system is in the borderline of being a Lyman limit system and a sub-DLA. Moreover, the ionization parameter determined from the observed $\frac{\text{SiIV}}{\text{SiII}}$ ratio was $\log U > -2.75$, which is consistent with the value determined from the observed $\frac{\text{AlIII}}{\text{AlII}}$ ratio.

For the system at $z = 2.635$ with $\log N_{\text{HI}} = 19.50 \pm 0.12$, we used grids of models in the range $1.5 > \log n_{\text{H}} > -3$ to calculate the predicted column density ratios $\log \frac{\text{AlIII}}{\text{AlII}}$ as well as $\log \frac{\text{SiIV}}{\text{SiII}}$. Comparing the prediction to the observed Al III/Al II ratio gave $\log U = -5.01$ and $\log n_{\text{H}} = 0.1$ (see Fig. 11). The

ionization corrections are quite small ($\sim \pm 0.02$ dex) for O, Si, Fe, and Al, and modest (0.12 dex) for Zn (see Table 10). Since Si II appears to be saturated, the ionization parameter constrained from $\log \frac{\text{SiIV}}{\text{SiII}}$ is $\log U < -3.1$ which is consistent with the estimate from the observed $\frac{\text{AlIII}}{\text{AlII}}$ ratio. Similarly, for the system at $z = 2.236$ with $\log N_{\text{HI}} = 19.75 \pm 0.10$, we used grids of models in the range $0.5 > \log n_{\text{H}} > -3$, calculating the predicted column density ratio $\log \frac{\text{AlIII}}{\text{AlII}}$. This gave $\log U = -3.83$ and $\log n_{\text{H}} = -1.0$ (see Fig. 12). The ionization corrections for this system are quite small ($\sim \pm 0.1$ dex for Si, Fe, and Zn) and the correction for O is again negligible (< 0.01 dex) (see Table 11). Since Al II appears saturated, the ionization parameters for both of these absorbers are likely to be lower than the values listed above and the corrections for absorbers are likely to be even smaller. The ionization corrections for all of these absorbers are listed in Tables 9, 10, and 11. It is clear that the ionization corrections for the elements we use as metallicity indicators are either negligible (for O) or small (~ 0.1 dex for Zn). These results are in agreement with past studies of ionization in sub-DLAs (e.g. Dessauges-Zavadsky et al. 2003; Meiring et al. 2009; Cooke et al. 2011; Som et al. 2015).

5.2 Metallicity, relative abundances, and dust

In general, the sub-DLA global mean metallicity appears to be higher than that of DLAs in the redshift range

Table 9. Total and relative element abundances in the $z_{abs} = 2.539$ absorber along the sight line to J1106-1731, before and after ionization correction.

Element	[X/H] _{NoIC}	Correction	[X/H] _{IC}	[X/O] _{NoIC}	[X/O] _{IC}
O	-1.30 ± 0.12	+0.03	-1.27 ± 0.12		
Si	0.05 ± 0.12	-0.87	-0.82 ± 0.12	1.35 ± 0.04	0.45 ± 0.04
Fe	-0.78 ± 0.14	-0.38	-1.16 ± 0.14	0.52 ± 0.08	0.11 ± 0.08
Al	-0.03 ± 0.14	-1.01	-1.04 ± 0.14		

Table 10. Total and relative element abundances in the $z_{abs} = 2.635$ absorber along the sight line to J1244+1129, before and after ionization correction.

Element	[X/H] _{NoIC}	Correction	[X/H] _{IC}	[X/O] _{NoIC}	[X/O] _{IC}
O	> 0.40	-0.004	> 0.40		
Si	0.23 ± 0.15	-0.02	0.21 ± 0.15		
Fe	-0.85 ± 0.13	-0.02	-0.87 ± 0.13		
Al	0.28 ± 0.18	0.02	0.30 ± 0.18		
Zn	0.28 ± 0.12	0.12	0.40 ± 0.12		

Table 11. Total and relative element abundances in the $z_{abs} = 2.236$ absorber along the sight line to J1614+1448, before and after ionization correction.

Element	[X/H] _{NoIC}	Correction	[X/H] _{IC}	[X/O] _{NoIC}	[X/O] _{IC}
O	-0.69 ± 0.17	-0.01	-0.70 ± 0.17		
Si	-0.48 ± 0.11	-0.11	-0.59 ± 0.11	0.21 ± 0.14	0.11 ± 0.14
Fe	-0.71 ± 0.11	-0.09	-0.80 ± 0.11	-0.02	-0.10
Al	> -0.84	0.09	> -0.75		

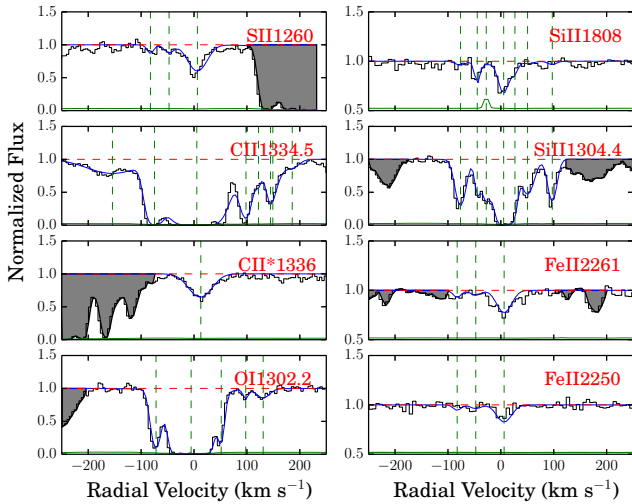


Figure 2. Velocity plots for metal lines for the absorber at $z = 2.173$ in the sight line to J1106-1731. In each panel, the observed data are shown in black and the fitted profiles are shown in blue. The green line at the bottom of each panel shows the 1σ error in the normalized flux. The placement of continuum is shown by the horizontal dashed red line. The vertical dashed lines in green show the different velocity components included in the profile fits. The shaded regions are the telluric and unrelated absorption features.

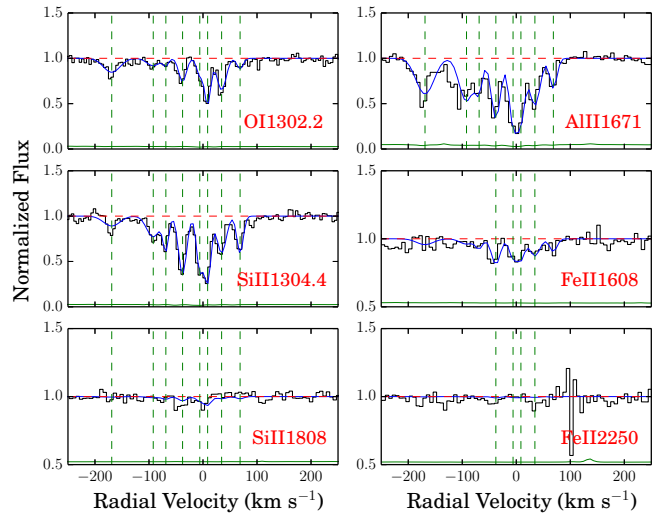


Figure 3. Same as Fig. 2 but showing the Voigt profile fits for the metal lines in the absorber at $z = 2.539$ in the sight line to J1106-1731.

$0 \lesssim z \lesssim 3$ for which both DLA and sub-DLA observations are available (e.g. Som et al. 2013, 2015). As sulfur, oxygen, and zinc are weakly depleted on interstellar dust grains, they are believed to probe nearly dust-free or intrinsic metallicity. The zinc-based metallicity for the absorber at

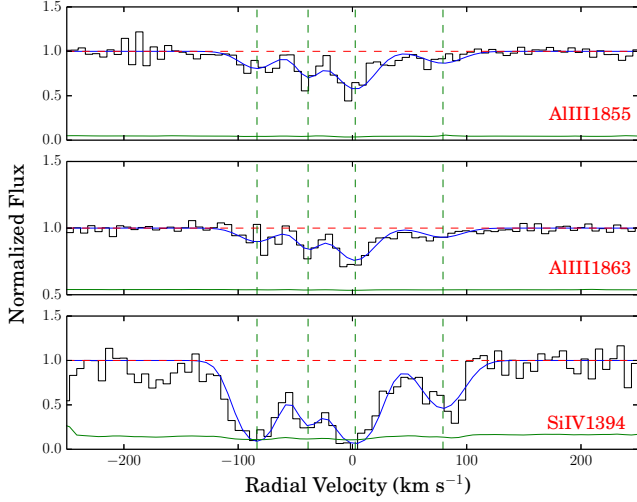


Figure 4. Same as Fig. 3 but showing the Voigt profile fits for the higher ions in the absorber at $z = 2.539$ in the sight line to J1106-1731.

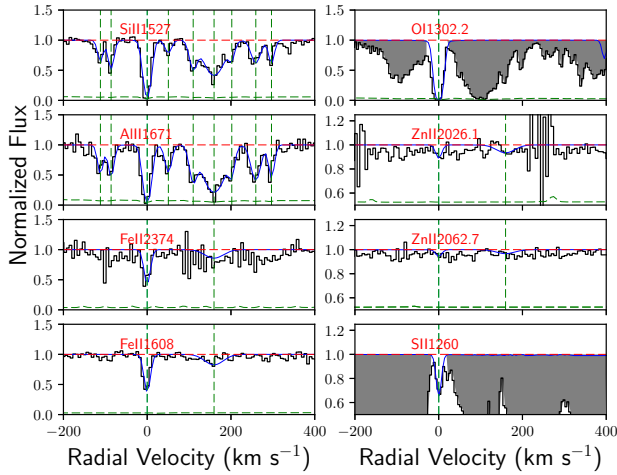


Figure 5. Velocity plots for metal lines for the absorber at $z = 2.635$ in the sight line to J1244+1129. In each panel, the observed data are shown in black and the fitted profiles are shown in blue. The green line at the bottom of each panel shows the 1σ error in the normalized flux and the placement of continuum is shown by the horizontal dashed red line. The vertical dashed lines in green show the different velocity components included in the profile fits. The shaded regions are the telluric and unrelated absorption features.

$z=2.635$ along the sight line to J1244+1129 is supersolar ($[\text{Zn}/\text{H}]=0.40\pm0.12$). Similarly, sulfur-based metallicity for the absorber at $z=2.173$ along the sight line to J1106-1731 is $[\text{S}/\text{H}]=-0.50\pm0.11$. The oxygen-based metallicities for the absorbers at $z=2.539$ and at $z=2.236$ along the sight lines to J1106-1731 and J1614+1448 are estimated to be $[\text{O}/\text{H}]=-1.27\pm0.12$ and $[\text{O}/\text{H}]=-0.70\pm0.17$, respectively. This shows that all of our 4 sub-DLAs are found to be metal-rich

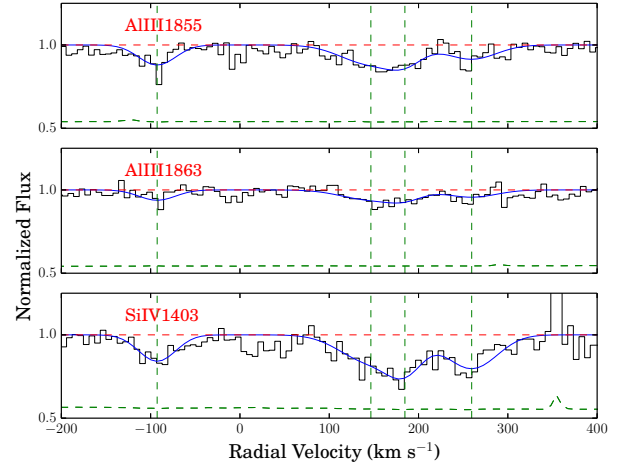


Figure 6. Same as Fig. 5 but showing the Voigt profile fits for the higher ions in the absorber at $z = 2.635$ along the sight line to J1244+1129.

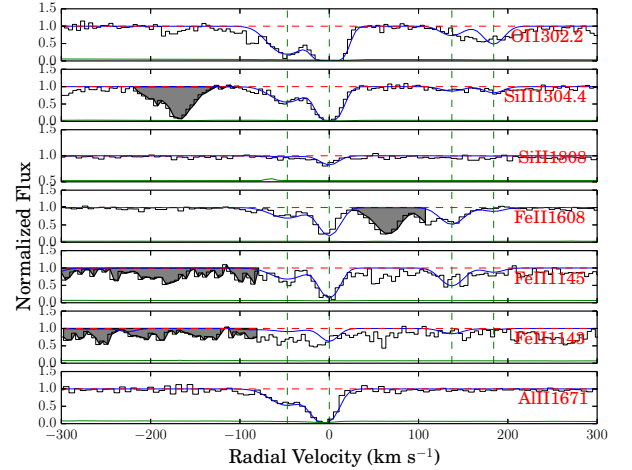


Figure 7. Velocity plots for metal lines for the absorber at $z = 2.236$ in the sight line to J1614+1448. In each panel, the observed data are shown in black and the fitted profiles are shown in blue. The green line at the bottom of each panel shows the 1σ error in the normalized flux and the placement of continuum is shown by the horizontal dashed red line. The vertical dashed lines in green show the different velocity components included in the profile fits. The shaded regions are the telluric and unrelated absorption features.

based on the weakly depleted elements compared to typical DLAs at comparable redshifts.

Si and Fe are found to be under-abundant relative to Zn, with $[\text{Si}/\text{Zn}] = -0.19$ and $[\text{Fe}/\text{Zn}] = -1.27$ for the absorber at $z_{\text{abs}}=2.635$ along the sight line to J1244+1129. Similarly, Fe is found to be under-abundant relative to S, with $[\text{Fe}/\text{S}] = -0.16$ for the absorber at $z_{\text{abs}}=2.173$ along the sight line to J1106-1731. Such $[\text{Si}/\text{Zn}]$, $[\text{Fe}/\text{Zn}]$, and $[\text{Fe}/\text{S}]$

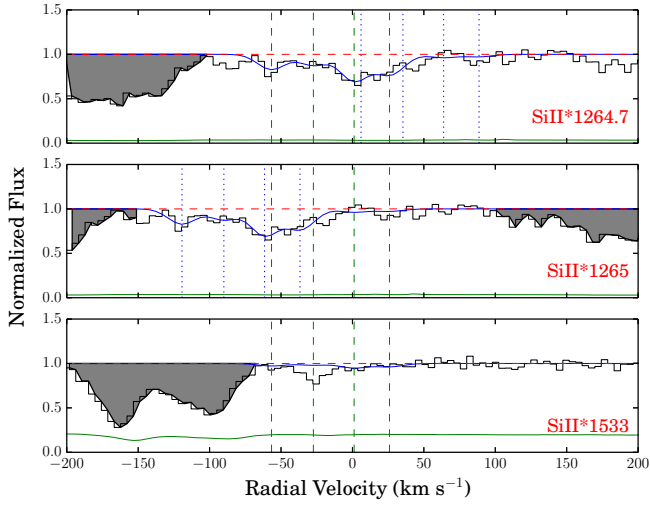


Figure 8. Velocity plots for Si II* $\lambda 1264.7$, Si II* $\lambda 1265$, and Si II* $\lambda 1533$ lines for the absorber at $z = 2.236$ in the sight line to J1614+1448. The vertical dashed lines in green show the different velocity components included in the profile fits. The dotted lines in blue in the upper panel show the components corresponding to Si II* $\lambda 1265$ and the dotted lines in blue in the middle panel show the components corresponding to Si II* $\lambda 1264.7$. The shaded regions are the telluric and unrelated absorption features.

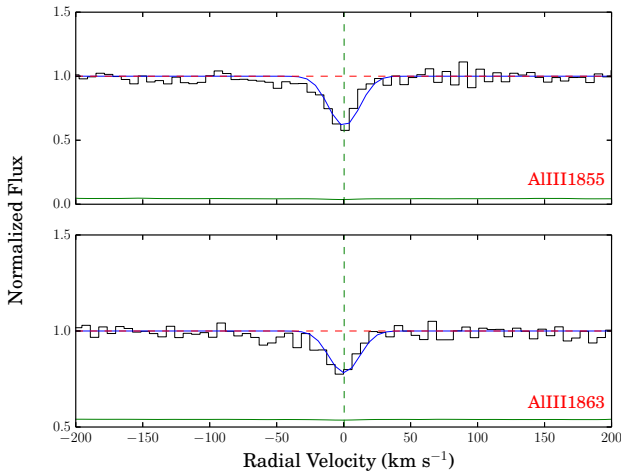


Figure 9. Same as Fig. 7 but showing the velocity plots for higher ions in the absorber at $z = 2.236$ along the sight line to J1614+1448.

values can be expected if the refractory elements (elements with higher condensation temperature) such as Si and Fe are depleted onto dust grains more severely than the volatile elements (elements with lower condensation temperature) such as Zn and S. However, it is interesting to note that the Si is overabundant in comparison to S for the absorber at $z=2.173$, with $[\text{Si}/\text{S}] = 0.23 \pm 0.06$. Such a high $[\text{Si}/\text{S}]$ value is unusual, given that $[\text{Si}/\text{S}]$ is often either zero (in the ab-

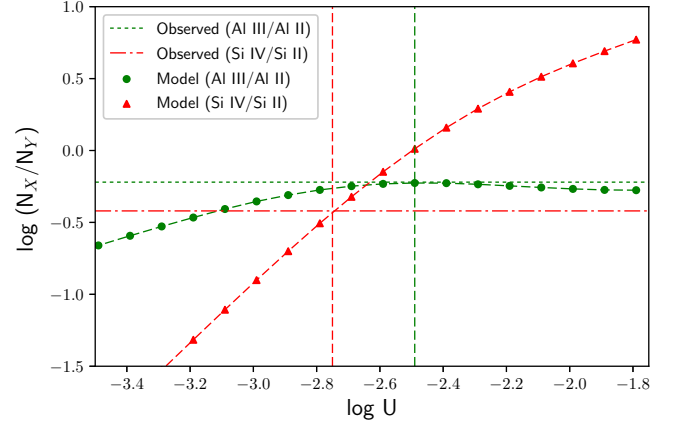


Figure 10. Results of Cloudy photo-ionization calculations for the absorber at $z = 2.539$ in the sight line to J1106-1731, showing the ion ratios as a function of the ionization parameter U . The vertical lines correspond to the value of U implied by the observed $\frac{\text{Si IV}}{\text{Si II}}$ and $\frac{\text{Al III}}{\text{Al II}}$ ratios (indicated by the horizontal lines in red and blue respectively).

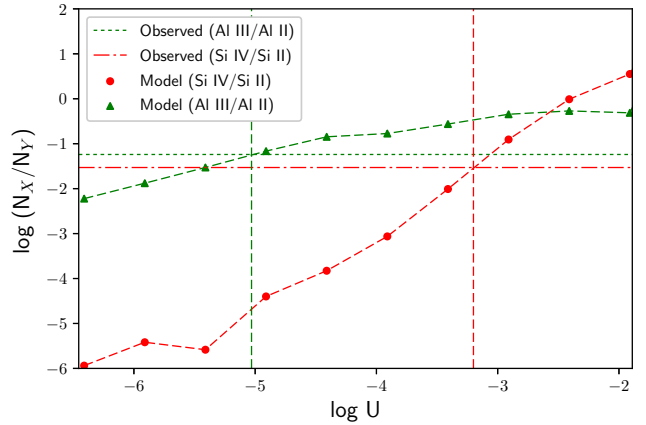


Figure 11. Same as Fig. 10 but showing the results of Cloudy photo-ionization calculations for the absorber at $z = 2.635$ in the sight line to J1244+1129.

sence of dust depletion) or negative (in the presence of dust depletion).

5.3 Gas Kinematics

As suggested by some simulations, the velocity width of absorption lines could be related to the gravitational potential well of the absorption system's host galaxy (e.g. Prochaska & Wolfe 1997b; Haehnelt, Steinmetz & Rauch 1998; Pontzen et al. 2008). Ledoux et al. (2006), Møller et al. (2013), and Péroux et al. (2003a) reported a relation between velocity width vs. metallicity. One potential interpretation of this relation is in terms of the stellar mass vs. metallicity relation (MZR) of galaxies, assuming galaxy luminosity scales with the dark matter

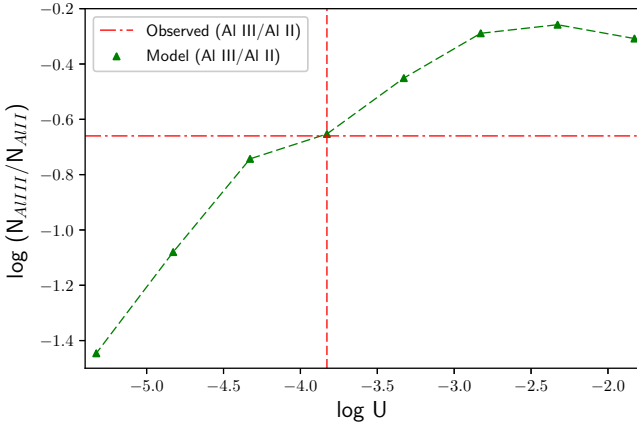


Figure 12. Same as Fig. 10 but showing the results of Cloudy photo-ionization calculations for the absorber at $z = 2.236$ in the sight line to J1614+1448.

halo mass. Under this assumption, the velocity width of the low-ionization absorption lines may be used as a proxy for the stellar mass of these systems, which has been difficult to measure. While many previous studies suggest a correlation between mass and metallicity, Zwaan et al. (2008) show that the velocity width and mass do not correlate well in local analogues of DLAs. We measured the velocity width values for the systems in our sample following the analysis of Wolfe & Prochaska (1998). The velocity width for a system was measured using an absorption profile from a low-ion transition seen in the system. High-ionization lines are not suitable for this analysis as their velocity widths are more likely to be dominated by large-scale thermal motions in the gas.

The Si II and Fe II absorption lines in the $z_{abs} = 2.173$ and $z_{abs} = 2.539$ sub-DLAs along the sight line to J1106-1731 are spread over velocity widths of 157 km s^{-1} and 215 km s^{-1} , respectively (Fig. 13 and Fig. 14). The observed values of metallicities for these two systems are within $\sim 2\sigma$ of the expected values based on the metallicity-velocity relation $[X/H] = (0.88 \pm 0.08) \log \Delta V_{90} - (1.86 \pm 0.16)$ observed for lower redshift sub-DLAs (Som et al. 2015). Similarly, the Fe II absorption for the $z_{abs} = 2.635$ sub-DLA along the sight line to J1244+1129 has a velocity width of 188.2 km s^{-1} , which is also consistent with the prediction from the metallicity-velocity relation (see Fig. 16). Moreover, the Si II absorption in the $z_{abs} = 2.236$ sub-DLA along the sight line to J1614+1448 is spread over velocity width of 163 km s^{-1} (see Fig. 15). The metallicity of this absorber (-0.70 ± 0.17) is somewhat lower than the value one can expect from the MZR relation for sub-DLAs from Som et al. (2015). However, we note that the contribution of Si II $\lambda 1808$ beyond $\sim 80 \text{ km s}^{-1}$ to the total absorption fraction is very small. If we neglect these two smaller components beyond $\sim 80 \text{ km s}^{-1}$, the observed velocity width of 62.7 km s^{-1} is consistent with the observed metallicity of -0.70 ± 0.17 .

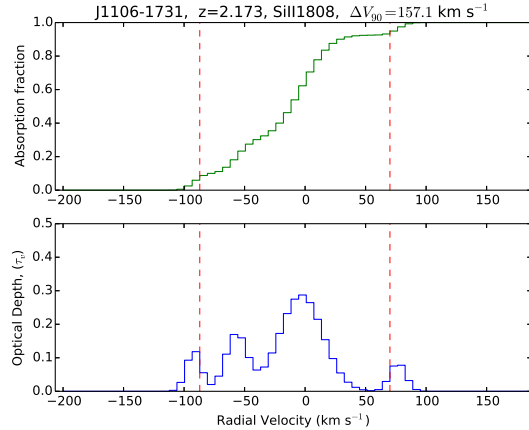


Figure 13. Plot showing absorption fraction vs. radial velocity (upper panel) and optical depth vs. radial velocity (lower panel) for the sub-DLA at $z_{abs} = 2.173$ along the sight line to J1106-1731. The names of the sight line, redshift of the absorber, name of the metal line used, and the estimated value of the velocity width are listed in the top panel. The velocity dispersion is estimated as the length of the radial velocity within which 90 percent of the cumulative optical depth is contained. The left and right vertical dashed lines in red are drawn corresponding to 5 percent and 95 percent of cumulative optical depth.

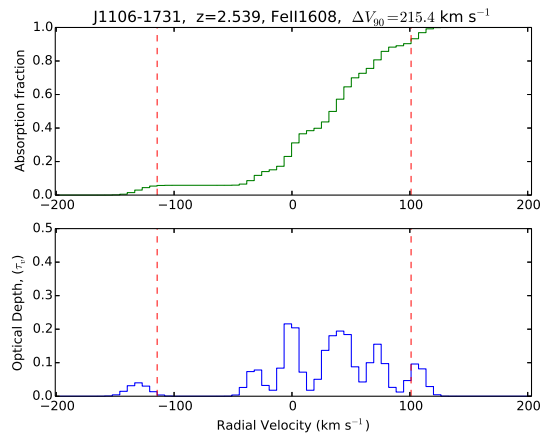


Figure 14. Same as Fig. 13.

5.4 Constraints on Electron Densities

Fine structure lines of C II* and Si II* provide constraints on the electron density by assuming equilibrium between collisional excitation and spontaneous radiative de-excitation for an assumed gas temperature (e.g. Srianand & Petitjean 2000). Si II* absorption has been detected in gamma-ray burst afterglows (e.g. Savaglio 2012), however, it is rare in quasar absorbers. We detect Si II* absorption in the sub-DLA at $z_{abs} = 2.236$ along the sight line to J1614+1448. We performed Voigt profile fitting of Si II* $\lambda\lambda 1264, 1265, 1533$ simultaneously and determined $\log N_{\text{SiII}^*}$ to be 12.77 ± 0.12 . We assumed the Si II collisional excitation rate $C_{12} = 3.32 \times 10^{-7} (T/10^4)^{-0.5} \exp(-413.4/T) \text{ cm}^3 \text{ s}^{-1}$, and the Si II* spontaneous radiative de-excitation rate $A_{21} = 2.13 \times 10^{-4} \text{ s}^{-1}$ (e.g. Srianand & Petitjean 2000).

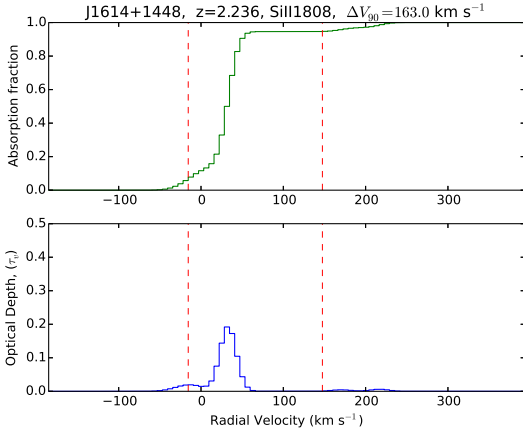


Figure 15. Same as Fig. 13. We note that the contribution of Si II $\lambda 1808$ to the total absorption fraction beyond ~ 80 km s $^{-1}$ is very small. If we neglect two smaller components beyond ~ 80 km s $^{-1}$, we get velocity width of 62.7 km s $^{-1}$.

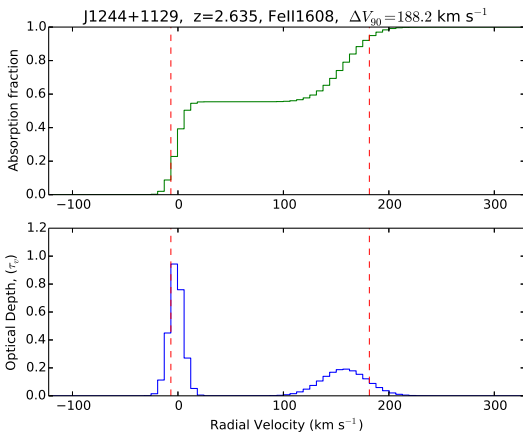


Figure 16. Same as Fig. 13.

The electron density is then given by $n_e = (N_{\text{SiII}^*} / N_{\text{SiII}}) A_{21}/C_{12}$. Given the temperature dependence of C_{12} , we consider two illustrative cases of $T = 500$ K and $T = 7000$ K. We obtained $n_e = 3.18$ cm $^{-3}$ and $n_e \dot{D} = 5.53$ cm $^{-3}$, respectively, for assumed temperatures $T = 500$ K and $T = 7000$ K. These values are much higher than the median value $n_e = 0.0044 \pm 0.0028$ cm $^{-3}$ found in DLAs (e.g. Neeleman et al. 2015) and also higher than the range of electron density values (0.007-0.047 cm $^{-3}$) found in the H $_2$ -bearing high- z DLAs (e.g. Srianand et al. 2005). In fact, our above-mentioned estimates of the electron density in the sub-DLA toward J1614+1448 are higher than even the values found in some super-DLAs (e.g. Kulkarni et al. 2012, 2015; Noterdaeme et al. 2015), the highest of which is in the range $n_e = 0.53$ -0.91 cm $^{-3}$.

Moreover, we were able to detect C II * λ 1335.7 for the absorber at $z = 2.173$ in the sight line to J1106-1731. However, as most of the components of C II λ 1334 were saturated for this system, we were able to put only an upper limit on the electron density, n_e . Again, we estimated the

electron density $n_e = (N_{\text{CII}^*} / N_{\text{CII}}) A_{21}/C_{12}$, by assuming equilibrium between the collisional excitation and the radiative de-excitation of C II, where, $A_{21} = 2.29 \times 10^{-6}$ s $^{-1}$ (e.g. Nussbaumer & Storey 1981). The collision rate coefficient is given by $C_{12}(T) = [8.63 \times 10^{-6} \Omega_{12} / (g_1 T^{0.5})] \exp(-E_{12}/kT)$ (e.g. Wood & Linsky 1997), where, $g_1 = 2$, $E_{12} = 1.31 \times 10^{-14}$ erg, and the collision strength Ω_{12} depends on temperature. We were able to put upper limits of $n_e < \dot{D} 0.18$ cm $^{-3}$ and $n_e \dot{D} < 0.58$ cm $^{-3}$, respectively, for assumed temperatures $T = 500$ K and $T = 7000$ K. These values are comparable to the median value $n_e = 0.0044 \pm 0.0028$ cm $^{-3}$ found in DLAs (e.g. Neeleman et al. 2015).

5.5 Cooling Rate

Wolfe, Gawiser & Prochaska (2003) developed a technique to infer the star formation rate per unit area for individual damped Lyman-alpha systems. In this technique, the [C II] 158 μ m cooling rate is inferred from the C II λ 1335.7 absorption line in the neutral gas producing the damped Ly-alpha absorption. The C II * λ 1335.7 transition arises from the excited $^2P_{3/2}$ state in C $^+$. A spontaneous photon decay of the $^2P_{3/2}$ state to the $^2P_{1/2}$ state results in [C II] 158 μ m emission, which is the principal coolant of neutral gas in the Galactic ISM (e.g. Wright 1991). At thermal equilibrium, the cooling rate equals the heating rate, which makes it possible to calculate the star formation rate per unit area. The cooling rate can be expressed as $l_c = N_{\text{CII}^*} E_{ul} A_{ul} / N_{\text{HI}}$, where E_{ul} and A_{ul} denote the energy and coefficient for spontaneous photon decay for the transition from the $^2P_{3/2}$ state to $^2P_{1/2}$ (e.g. Pottasch et al. 1979). Using $A_{ul} = 2.29 \times 10^{-6}$, we estimate $l_c = 1.20 \times 10^{-26}$ erg s $^{-1}$ per H atom for the absorber at $z = 2.173$ in the sight line to J1106-1731, suggesting a higher star formation rate density in this sub-DLA than the typical star formation rate density for DLAs at similar redshifts from Wolfe, Gawiser & Prochaska (2003). The cooling rate versus H I column density data for the sub-DLA from this work along with the corresponding measurements for DLAs from Wolfe, Gawiser & Prochaska (2003), sub-DLAs from Som et al. (2013), and for interstellar clouds in the Milky Way adopted from Lehner, Wakker, & Savage (2004) are plotted in Fig. 17. While our value of the cooling rate is lower than that for some other sub-DLAs and for low-velocity H I gas in the Milky Way ISM, it is higher than the cooling rate for all the DLAs from Wolfe, Gawiser & Prochaska (2003).

5.6 Search for the CO molecules

Most of the Lyman and Werner band absorption lines of H $_2$ for all the absorbers in our sample are not covered by the spectra. While a few of these lines are covered, the S/N in this region is very low and, furthermore, these lines are blended with the Lyman-alpha forest. For all of our absorbers, several lines of CO were covered, but they were not detected. We estimate 3σ upper limits of $\log N_{\text{COJ}0} < 13.68$ and $\log N_{\text{COJ}0} < 14.05$, respectively, from the non-detections of COJ0 λ 1477.6 and COJ0 λ 1544.4 lines.

Moreover, we search for molecules by combining the absorption spectra for all of our absorbers near the position of

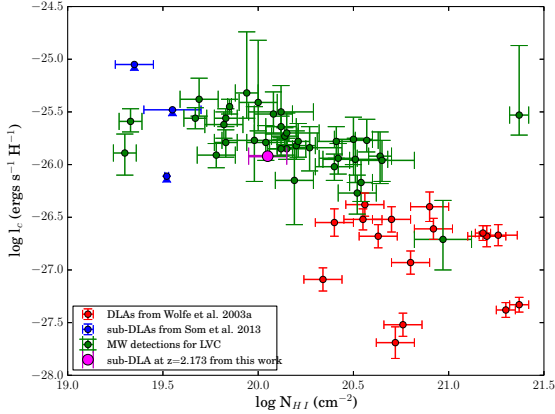


Figure 17. Inferred C II* spontaneous emission rate per H atom, l_c , versus H I column density. The red points denote the sample of QSO DLAs in [Wolfe, Gawiser & Prochaska \(2003\)](#). The green points represent the measurements for low-velocity interstellar H I clouds in the Milky Way compiled in [Lehner, Wakker, & Savage \(2004\)](#). The point in magenta represents a sub-DLA at $z=2.173$ along the sight line to J1106-1731 from this work. The blue points denote the lower limits for the sub-DLAs from [Som et al. \(2013\)](#).

similar molecules in order to see if there exists any systematic absorption signatures. To accomplish this, we converted the absorption spectra for all the absorbers to rest frame and made the velocity plots for each molecule. Fig. 18 shows the velocity plots for the molecular lines COJ0 λ 1477.6, COJ0 λ 1509.7, and COJ0 λ 1544.4 as going from top to bottom. The subplots are in the increasing order of redshifts as going from top to bottom. There is a slight hint of absorption in the CO 1544.448 line for the $z = 2.635$ system, but no corresponding absorption is seen in the stronger CO 1477.565 and 1509.748 lines. Therefore, It is clear from these plots that we are not able to detect any systematic features as an evidence of CO molecules. Higher S/N and lower wavelength spectra of our sub-DLAs are essential to perform more sensitive searches for H₂ and CO.

6 CONCLUSIONS

In this paper, we have presented high-resolution absorption spectra of four sub-DLAs at $2.173 < z_{abs} < 2.635$, increasing the existing sample for undepleted elements in sub-DLAs and thus improving the constraints on the cosmic metal evolution. We find a spread in the metallicities, which range from -1.27 dex to $+0.40$ dex. These observations suggest that metal-rich sub-DLAs appear at high redshift as well, supporting the conclusion made by [Som et al. \(2013\)](#). We are also able to put constraints on the electron density by assuming equilibrium between collisional excitation and spontaneous radiative de-excitation for an assumed gas temperature using fine structure lines of C II* and Si II* for two of the sub-DLAs. These values are much higher than the values found in DLAs (including H₂-bearing DLAs) and even in super-DLAs. We estimate the cooling rate for a sub-DLA at $z = 2.173$ in the sight line to J1106-1731 using C II* λ 1335.7 line to be $l_c = 1.20 \times 10^{-26}$ erg s⁻¹ per H atom, suggesting higher SFR density in this sub-DLA than the

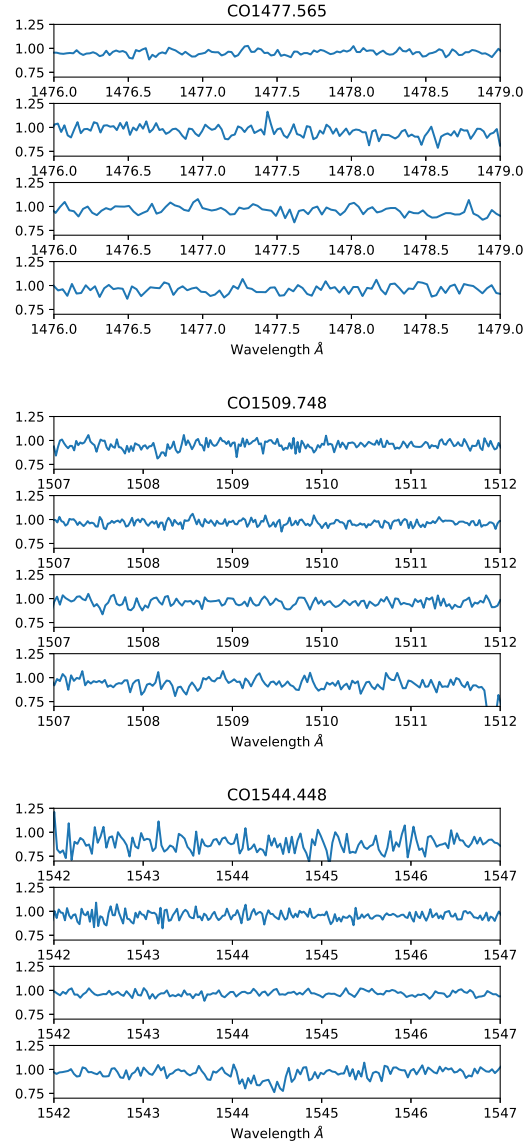


Figure 18. Plot showing the positions of molecular lines of CO at rest frame for all of the absorbers. The subplots are in increasing order of redshift going from top to bottom (from $z=2.173$ to $z=2.635$).

typical SFR density for DLAs at similar redshifts. We also study the metallicity versus velocity dispersion relation for our absorbers and compare the values with those from the literature. Most of the absorbers follow the trend one can expect from the mass versus metallicity relation for sub-DLAs from literature. Finally, although our spectra either do not cover or have very low S/N in the locations of H₂ lines, we are able to put limits on the column density of CO from the non-detections of various strong electronic transitions. We estimate 3σ upper limits of $\log N_{COJ0} < 13.68$ and $\log N_{COJ0} < 14.05$, respectively, from the non-detections of COJ0 λ 1477.6 and COJ0 λ 1544.4 lines. We emphasize the need of higher S/N and lower wavelength spectra of our sub-DLAs to obtain more definitive determinations of H₂ and CO contents.

ACKNOWLEDGEMENTS:

SP, VPK, and DS thank the helpful staff of Las Campanas Observatory for their assistance during the observing runs. SP and VPK gratefully acknowledge support from NASA grant NNX17AJ26G (PI Kulkarni) and NSF grant AST-0908890 (PI Kulkarni).

REFERENCES

- Asplund M., Grevesse N., Sauval A. J., Jacques S. P. 2009, *ARA&A*, 47, 481
- Berg T. A. M. et al. 2019, *MNRAS*, 488, 3
- Cashman F. H., Kulkarni V. P., Kisieliu R., Ferland G. J., Bogdanovich P. 2017, *APJ*, 230, 8
- Cooke R., Pettini M., Steidel C. C., Rudie G., Nissen P. E. 2011, *MNRAS*, 417, 1534
- Dessauges-Zavadsky M., Peroux C., Kim T. S., D’Odorico S., McMahon R. G. 2003, *MNRAS*, 345, 447
- Ferland G. J., Porter R. L., van Hoof P. A. M., et al. 2013, *RMxAA*, 49, 137
- Haehnelt M. G., Steinmetz M., Rauch M., 1998, *ApJ*, 495, 647
- Jorgenson R. A., Murphy M. T., Thompson R. 2013, *MNRAS*, 435, 482
- Khare P., Kulkarni V. P., Péroux C., York D. G., Lauroesch J. T., Meiring J. D., 2007, *A&A*, 464, 487
- Khaire V. & Srianand R., 2019, *MNRAS*, 484, 4174
- Kulkarni G., Rollinde E., Hennawi, Joseph F., Vangioni, E. 2013, *ApJ*, 772, 93
- Kulkarni, V. P., Fall S. M., Truran J. W. 1997, *ApJ*, 484L, 7
- Kulkarni V. P. & Fall S. M. 2002, *ApJ*, 580, 732
- Kulkarni V. P., Fall S. M., Lauroesch J. T., York D. G., Welty D. E., Khare P., Truran J. W., 2005, *ApJ*, 618, 68
- Kulkarni V. P., Khare P., Péroux C., York D. G., Lauroesch J. T., Meiring J. D., 2007, *ApJ*, 661, 88
- Kulkarni V. P., Khare P., Som D., Meiring J., York D. G., Péroux C., Lauroesch J. T. 2010, *NewA*, 15, 735
- Kulkarni V. P., Meiring J., Som D., et al. 2012, *ApJ*, 749, 176
- Kulkarni V. P., Som D., Morrison S., Péroux C., Quiret S., York D. G. 2015, *APJ*, 815, 24
- Ledoux, C., Petitjean, P., Møller P., Fynbo, J., Srianand R. 2006, *A&A*, 457, 71
- Lehner N., Wakker B. P., Savage B. D. 2004, *ApJ*, 615, 767
- Meiring J. D., Lauroesch J. T., Kulkarni V. P., Péroux C., Khare P., York D. G., & Crotts A. P. S. 2007, *MNRAS*, 376, 557
- Meiring J. D., Lauroesch J. T., Kulkarni V. P., et al. 2009, *MNRAS*, 397, 2037
- Møller P., Fynbo J. P. U., Ledoux C., Nilsson K. K. 2013, *MNRAS*, 430, 2680
- Morton D. C., 2004, *ApJS*, 151, 403
- Nagamine, K., Springel, V., Hernquist, L. 2004, *MNRAS*, 348, 421
- Nagamine, K.; Springel, V.; Hernquist, L. 2004, *MNRAS*, 348, 385
- Neeleman M., Prochaska J. X., & Wolfe, A. M. 2015, *ApJ*, 800, 7
- Noterdaeme P. et al. 2012, *A&A*, 547, L1
- Noterdaeme P., Srianand R., Rahmani H. et al. 2015, *A&A*, 577, 24
- Nussbaumer, H., & Storey, P. J. 1981, *A&A*, 96, 91
- Penprase B. E., Prochaska J. X., Sargent Wallace L. W., Toro-Martinez I., Beeler D. J. 2010, *ApJ*, 721, 1
- Péroux C., Dessauges-Zavadsky M., D’Odorico S., Kim Tae-Sun, McMahon R. G., 2003a, *MNRAS*, 345, 480
- Péroux C., McMahon R. G., Storrie-Lombardi L. J., Irwin M. J., 2003b, *MNRAS*, 346, 1103
- Pontzen A. et al., 2008, *MNRAS*, 390, 1349
- Pottasch S. R., Wesselius P. R., & van Duinen R. J. 1979, *A&A*, 74, L15
- Poudel S., Kulkarni V. P., Morrison S., Péroux C., Som D. Rahmani H., Quiret S. 2018, *MNRAS*, 473, 3559
- Poudel S., Kulkarni V. P., Cashman F. H., Frye, B., Péroux C., Rahmani H., Quiret S. 2019, *MNRAS*, 491, 1008
- Prochaska J. X., Wolfe A. M., 1997b, *ApJ*, 487, 73
- Prochaska J. X., Gawiser E., Wolfe A. M., Castro S., Djorgovski S. G. 2003a, *ApJ*, 595, L9
- Prochaska J. X., Gawiser E., Wolfe A. M., Cooke J., Gelino D. 2003b, *ApJ*, 147, 227
- Quiret S. et al. 2016, *MNRAS*, 458, 4074
- Rafelski M., Wolfe A. M., Prochaska J. X., Neeleman M., Mendez A. J., 2012, *ApJ*, 755, 89
- Rafelski M., Neeleman M., Fumagalli M., Wolfe A. M., Prochaska J. X. 2014, *ApJ*, 782, L29
- Rahmani H. et al. 2016, *MNRAS*, 463, 980
- Savaglio S., Rau A., Greiner J., et al. 2012, *MNRAS*, 420, 627
- Srianand R., & Petitjean P. 2000, *A&A*, 357, 414
- Srianand R., Petitjean P., Ledoux C., Ferland G., Shaw G. 2005, *MNRAS*, 362, 549
- Som D., Kulkarni V. P., Meiring J., York D. G., Péroux C., Khare P., Lauroesch J. T. 2013, *MNRAS*, 435, 1469
- Som D. et al. 2015, *ApJ*, 806, 25
- Wolfe A. M., Prochaska J. X., 1998, *ApJ*, 494, 15
- Wolfe A. M., Gawiser E., & Prochaska, J. X. 2003, *ApJ*, 593, 235
- Wolfe A. M., Howk J. C., Gawiser E., Prochaska J. X., & Lopez S. 2004, *ApJ*, 615, 625
- Wolfe A. M., Gawiser E., Prochaska J. X., 2005, *ARA&A*, 43, 861
- Wolfe A. M., Chen H. 2006, *ApJ*, 652, 981
- Wood B. E., & Linsky J. L. 1997, *ApJL*, 474, L39
- Wright E. L. 1991, *ApJ*, 375, 608
- Zafar T., Péroux C., Popping A., Milliard B., Deharveng J. M., Frank S. 2013, *A&A*, 556, 141
- Zwaan M., Walter F., Ryan-Weber E., Brinks E., de Blok W. J. G., Kennicutt R. C., 2008, *AJ*, 136, 2886

This paper has been typeset from a $\text{\TeX}/\text{\LaTeX}$ file prepared by the author.